

Influence of active layer thickness on photovoltaic performance of PTB7:PC70BM bulk heterojunction solar cell

Nidhi Sharma^a, Saral K. Gupta^a, Chandra Mohan Singh Negi^{b,*}

^a Department of Physics, Banasthali Vidyapeeth, Rajasthan, 304022, India

^b Department of Electronics, Banasthali Vidyapeeth, Rajasthan, 304022, India

ARTICLE INFO

Keywords:

Bulk heterojunction solar cell
Charge recombination
Leakage current
Ideality factor
Charge transport resistance
Photovoltaic performance

ABSTRACT

In this paper, we studied the effect of active layer thickness on the photovoltaic performance of inverted bulk heterojunction (BHJ) organic solar cell (OSC). The capacitance-voltage (C-V), dark current-voltage (I-V) and impedance spectroscopy (IS) analysis were carried out to explain the active layer thickness dependence on the photovoltaic performance. The OSC with an active layer thickness of 150 nm achieved the best power conversion efficiency (PCE) of 5.87%, while the OSC of 200 nm active layer thickness yielded the worst PCE. Reduction in the fill factor (FF) was the main reason for the reduction in the PCE at large active layer thickness. The dark I-V analysis revealed large defect density for the OSC with active layer thickness of 200 nm, which raised the charge recombination and leakage current and consequently reduced the FF. IS analysis predicted that the charge transport became the serious limitations for the OSC with 200 nm thick active layer, which can be attributed to the weakening of electric field as well as creation of field-free regions. It mainly caused a drastic drop in the fill factor by reducing the charge collection efficiency, consequently deteriorated the photovoltaic performance.

1. Introduction

The sun is an uncontaminated and unlimited natural energy resource that might help in mitigating the crisis of energy all over the globe. Additionally, The harness of solar energy can be a powerful approach to cope the looming problem of global warming, mainly if it can adopted at vast scale. Currently, silicon solar cells dominate the photovoltaic market, owing to the excellent electrical properties and matured processing technologies [1]. Nevertheless, the higher costs of silicon based solar cells have prevented them to significantly contribute as an energy source worldwide. Hence, it becomes a necessity to explore some cost effective photovoltaic materials. In this context, solution processed organic solar cells (OSCs) and organic-inorganic hybrid solar cells have shown the huge prospective for the inexpensive alternative of silicon solar cell [2–5]. Their benefits including, cost-effective manufacturing, flexibility, light weight, and facile processing has made them a state of the art technology of interest in upcoming years [6]. OSCs have also tremendously progressed in terms of power conversion efficiency (PCE) in last few years [7,8]. The development of solar cells with high PCE has a great importance, since it directly affects the ultimate cost of electricity.

Poly (3-hexylthiophene) (P3HT) is one of most widely used polymers for applications in all kind of organic based electronic devices [9]. It is also investigated extensively as a donor material in bulk heterojunction (BHJ) OSCs. P3HT is being exploited as the standard absorber material in OSCs since several years. However, its large band gap (~1.9 eV) restricts the absorption range to <600 nm, which

* Corresponding author.

E-mail address: nchandra@banasthali.in (C.M. Singh Negi).

limits the maximum achieved PCE of OSC up to 5% [10]. Copolymers formed through the alternative placement of benzodithiophene (BDT) and thieno [3,4-b]thiophene units has emerged as the potential absorbers for OSC appliances in recent years [11]. The thieno[3,4-b]thiophene units as a result of stabilizing the backbone's quinoidal structure reduces the polymer's energy gap to 1.6 eV. Moreover, the ester substituted thieno [3,4-b] thiophene enhances the polymer solubility and oxidative stability along with the firm, resulting in better hole mobility. Based on the fluorinated thieno [3,4-b] thiophene family, the poly[(4,8-bis-(2-ethylhexyloxy)-benzo(1,2-b:4,5-b') dithiophene)-2,6-diyl-alt-(4-(2ethylhexyl)-3fluorothieno [3,4-b]thiophene-)-2-carboxylate-2-6-diyl)] (PTB7) as an electron donor in combination with [6,6]-phenyl C₇₁ butyric acid methyl ester (PC70BM) as electron acceptor has become the materials of immense interest for active layer in bulk heterojunction OSCs, and has demonstrated PCE far better than the P3HT:PCBM BHJ system [12,13].

Inverting the OSC design can offer various benefits over the standard design. Inverted device structure improve the air stability of OSCs by eliminating the need for use of poorly stable low work function materials and allows the use of air stable high work function metals, such as silver (Ag) [13,14]. In addition, the inverted design improve the PCE by enhancing the charge collection efficiency of the devices [15,16,17]. In contrast to the standard geometry, where ITO collect the holes and metal electrode collect the electrons, in inverted structure ITO collects the electrons and holes are collected by the metal electrode. Furthermore, the interfacial layers between the electrodes and polymer active layer are crucial in deciding the performance of OSCs, since the energy level alignment between the active layer and interfacial layers decides the charge extraction efficiency [15,18]. These interfacial buffer layers lead to optimum inverted OPVs electrode selectivity, resulting in higher PCE and lifetime.

The performance of organic solar cell vastly dependent on the active layer thickness of the cell [19,20]. Since, the active layer is main functional layer in OSCs, it absorb the incoming radiation from the sun and convert it into the excitons. The excitons subsequently diffuse towards the donor/acceptor interface and separate into the free electrons and holes. These free electrons and holes then transport to the respective electrodes and contribute to the photocurrent. During transport, the carriers may suffer recombination losses at the bulk as well as at the interfaces. Enlarging the active layer improve the absorption, however it might increases the charge transport hindrance and recombination losses. Therefore a balance between absorbance, charge transport and recombination must be required to achieve the high performance. In this study, we aim to optimize the PCE of OSCs by varying the thickness of the active layer. The impact of active layer thickness on the performance characteristics were examined in detail. The Inverted OSCs were fabricated with the architecture of ITO/ZnO/PTB7: PC70BM/Molybdenum tri-oxide (MoO₃)/Ag. ZnO layer was used as the electron transport (hole blocking) layer and MoO₃ layer was employed to serve as the hole transport (electron blocking) layer. PTB7:PC70BM solution was prepared in chlorobenzene (CB) solvent with diiodooctane (DIO) as a solvent additive. The addition of DIO in the blend solution is expected to enhance the morphology, leading to the improved charge transport, and charge extraction [11].

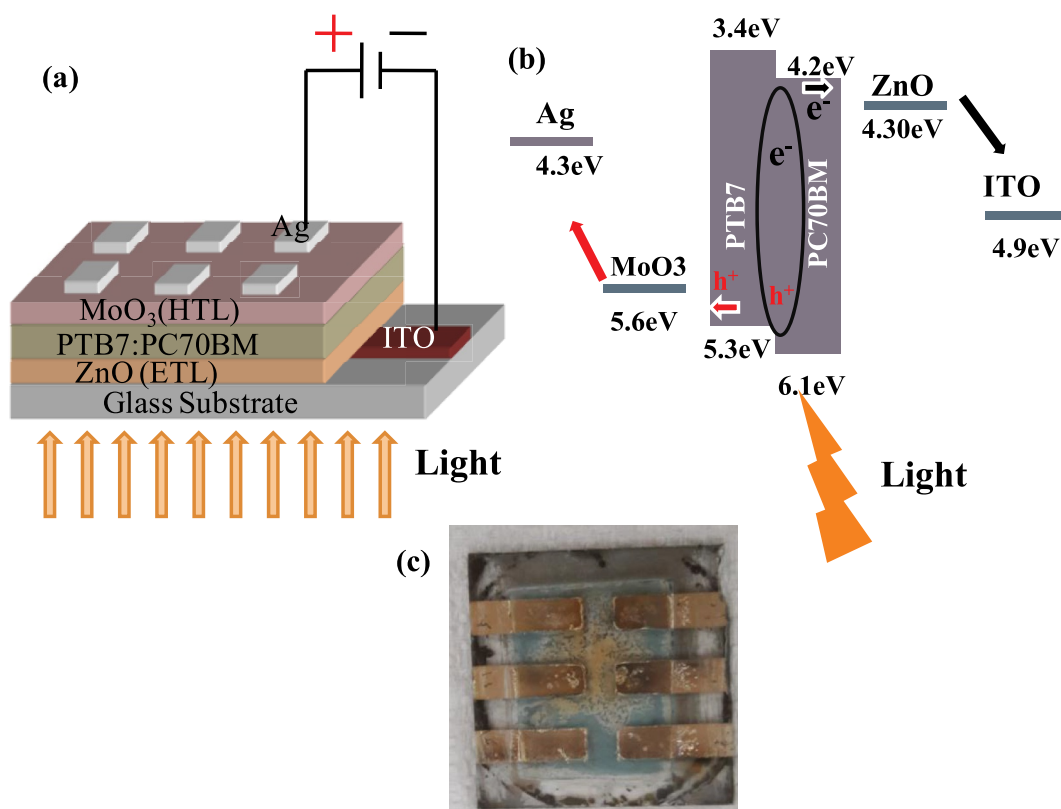


Fig. 1. (a) Schematic of the fabricated OSC with architecture of ITO/ZnO/PTB7:PC70BM/MoO₃/Ag, (b) energy level diagram of the materials used for fabrication of OSC, and (c) Photograph of fabricated device.

2. Experimental

2.1. Materials

PTB7 was received from Solarmer and PC70BM was purchased from Nano-c. Chlorobenzene (anhydrous, 99.8%) and 1,8-Diiodooctane (DIO, 98%), Tetrahydrofuran (THF, $\geq 99.9\%$), MoO_3 ($\geq 99.5\%$) and diethyl zinc solution (15 wt % in toluene) were procured from Sigma-Aldrich. The ITO coated pre-patterned glass substrates with a sheet resistance of $15\ \Omega/\text{square}$ were purchased from Xinyan technology limited. Ag (99.999%) was purchased from Alfa Aesar. All the chemicals were used as received.

2.2. Preparation methods

The OPV devices were fabricated on patterned ITO-coated glass substrate. Firstly, ITO substrates were etched by acid solution containing $\text{HCl}:\text{HNO}_3:\text{H}_2\text{O}$ (1:1:4) for 15–20 min. Then, substrates were cleaned by ultra bath sonication in detergent, deionized water, acetone and isopropanol consecutively for 10 min. The UV ozone treatment was then applied to ITO substrate for 20 min. Thereafter, ZnO solution prepared with Diethyl zinc and THF in 1:6 M ratios was spun coat over ITO substrate at 4000 rpm for 60 s followed by annealing at $120\ ^\circ\text{C}$ for 20 min. Afterwards, active layer composed of PTB7/PC70BM blends was spin-coated over the ZnO layer. The spin speed was set to 1000 rpm, 1500 rpm and 2000 rpm to realize the active layer thickness of 200 nm, 150 nm and 100 nm respectively. Solution of PTB7 and PC70BM with weight ratio of 1:1.5 and the concentration of 20 mg/ml was prepared in chlorobenzene and DIO (3 wt %) solvents via continuous stirring for 12 h. Subsequently, the samples were kept in vacuum for 30 min. Preparation of the samples and coating was performed in oxygen and moisture free nitrogen atmosphere inside the glove box. Afterwards, the samples were loaded into the vacuum chamber for the deposition of MoO_3 HTL and Ag electrode. MoO_3 (10 nm) was deposited on top of the active layer by thermal evaporation. Finally, Ag anode (100 nm) was deposited by thermal evaporation through a shadow mask under a pressure of 6×10^{-7} mbar. The resulting device has an area of approximately $0.01\ \text{cm}^2$. The schematic of fabricated OSC with architecture of ITO/ZnO/PTB7:PC70BM/ MoO_3 /Ag, energy level diagram of the materials used for fabrication of OSC, and photograph of fabricated device is presented in Fig. 1.

2.3. Characterization techniques

The thickness measurement of active layer was carried out using Near Normal Spectroscopic Reflectometer (HO-NNSR-01). The error in the thickness measurement was found to be 9.75, 4.1 and 3.9% for 100 nm, 150 nm and 200 nm active layer thickness, respectively. The absorption spectra of thin films deposited on glass substrate were recorded using PerkinElmer Lambda 750 UV–Vis–NIR Spectrophotometer. Current–Voltage (I–V) and Capacitance–Voltage (C–V) characteristics of OSCs were measured inside a nitrogen filled glove box using a computer controlled Keithley 4200 SCS (semiconductor characterization system) setup. The cells were individually illuminated using a LOT-Oriel Sun Simulator, housing a xenon lamp and using an AM 1.5G filter. The light is coupled to a solar cell device holder inside the glove box by a liquid light guide from Lot-Oriel. External Quantum efficiency has been measured using Enlitech (Enli-Technology Co. Ltd.) inside the glove box. The impedance measurements were carried out using an electrochemical workstation (Autolab PGSTAT30) with the frequency scan from 1 Hz to 1 MHz at 0 V DC in the dark. The amplitude of the AC voltage was set at 10 mV for all measurements. All the characterizations were performed at room temperature.

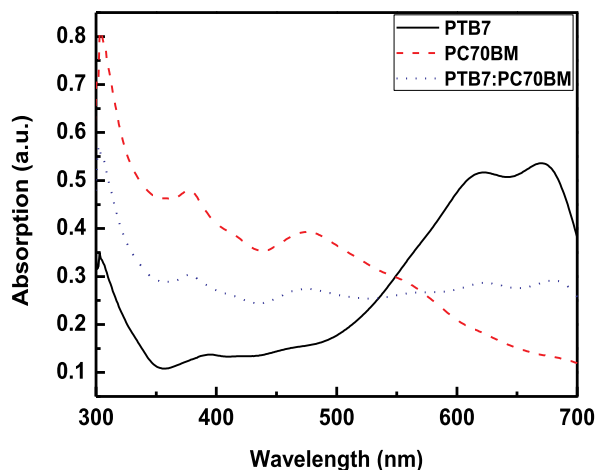


Fig. 2. UV/Vis/NIR absorption spectra for thin films of PTB7, PC70BM, and PTB7:PC70BM blends.

3. Results and discussions

The optical absorption spectra of pristine PTB7, pristine PC70BM and PTB7:PC70BM composite thin film is presented in Fig. 2. Thin film of PTB7 exhibits strong absorption observed from 550 to 700 nm with peak at 621 and 671 nm. On the other hand, PC70BM thin film displays strong absorption in the 300–550 nm range, which appears as opposite to that of PTB7 spectra. The absorption spectra of the resulting PTB7: PC70BM blend is appeared like a superposition of its constituent elements, which covers the wide range from 300 nm to 700 nm. The first peak in the absorption spectra of the composite at 325 nm originates from the interaction between 5-alkylthiophene-2-yl side chains and the second peak at 671 nm arises due to the intermolecular charge transfer absorption band. The similar results for the absorption spectra were reported earlier for the same materials [21,22]. The wider absorption range is obviously advantageous, since it can absorb the major portion of the solar spectrum, which can play a major role in improving the performance of the OPV.

The thickness dependent J-V characteristics of OSCs are depicted in Fig. 3(a). The performance parameters of the devices corresponding to the J-V curves are listed in Table 1. Table 1 clearly indicates that the active layer thickness has reasonable impact on device efficiency. The OSC with the active layer thickness (t) of 100 nm exhibits short circuit current density (J_{SC}), open circuit voltage (V_{OC}), fill factor (FF) and PCE of 11.55 mA/cm², 0.740 V, 61.9%, and 5.29%, respectively. As the thickness increased from 100 nm to 150 nm, the J_{SC} of the device increased to 18.90% accompanied with the slight improvement (1.35%) in V_{OC} , however the FF drops significantly from 61.9% to 56.9%. Among the devices under study, the device with $t = 150$ nm achieve the best PCE of 5.87%. With further increase in the t from 150 to 200 nm, J_{SC} , V_{OC} and FF deteriorated significantly, leading to decline in the PCE of OSC.

The observed improvement in the J_{SC} at $t = 150$ nm is due to the increase in the number of absorbed photons in comparatively thick active layer. Despite that the number of photons absorbed at $t = 200$ nm are comparatively larger than $t = 100$ nm and $t = 150$ nm, J_{SC} of the OSC decreases considerably. Increase in the active layer thickness, increases the chances of recombination, as the charge carriers have to travel comparatively longer pathway before reaching at the collecting electrodes. This variation in J_{SC} with thickness is consistent with the external quantum efficiency (EQE) response of the OSCs (Fig. 3(b)). The EQE indicates the efficiency to convert the incident photons into the charge carriers at the external circuit. EQE for all OSCs exhibits broad response from 300 to 800 nm. The EQE is nearly same for all the devices in longer wavelength spectral range. However, pronounced increase in EQE is observed for the OSC with $t = 150$ nm in the 360–560 nm wavelength region, which indicates that photo generated carriers are effectively extracted in the external circuit without much recombination, leading to the enhancement in J_{SC} [23]. As can be seen, the EQE reduces for OSC with $t = 200$ nm, particularly in the wavelength range from 360 to 680 nm, suggesting that increased carrier recombination had reduced the number of extracted charge carriers at large value of t .

The reduction in the V_{OC} at 200 nm can be correlated with the energy deficit due the increased recombination mechanisms. The equation which relates the energy deficit and V_{OC} can be written as [[24]].

$$V_{oc} = \frac{1}{e} (IP_{donor} - EA_{acceptor}) + \frac{mk_B T}{e} \ln \left(\frac{J_{sc}}{J_0} \right) \quad (1)$$

First part of the equation describes the difference between ionization potential of donor and acceptor material. m is the material related parameter, k_B is the Boltzmann's constant, e being the charge and J_0 is the reverse saturation current density.

The V_{OC} is limited by maximum separation of electron and hole quasi Fermi levels achieved under illumination condition. It was observed that the photo generated charge carriers increases the separation, while recombination mechanism decreases the separation between quasi Fermi levels. Thus, increase in the recombination mechanism, limits the V_{OC} of the OSC at $t = 200$ nm.

The drop in the FF with increase in the thickness of the active layer can be ascribed to the increase in the series resistance accompanied with the decrease in the shunt resistance with increase in the active layer thickness (Table 1). Increased series resistance

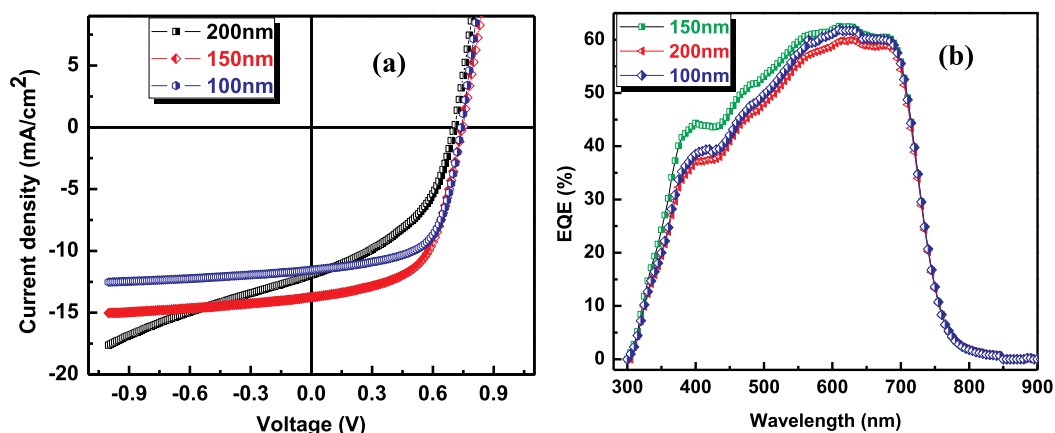


Fig. 3. (a) Current density–voltage characteristics of PTB7:PC70BM BHJ OSCs for different active layer thickness, and (b) corresponding EQE spectra.

Table 1

Photovoltaic parameters of PTB7:PC70BM BHJ OSCs with different active layer thickness under AM 1.5G solar illumination.

Device	FF (%)	V _{OC} (V)	J _{SC} (mA/m ²)	E _{FF} (%)	R _S (Ω)	R _{SH} (KΩ)
100 nm	61.9	.740	11.55	5.29	11.71	1.07
150 nm	56.9	.750	13.74	5.87	12.02	0.7092
200 nm	44.2	.710	11.00	3.75	18.7	0.2242

and decreased shunt resistance reduces the steepness of the slope, thus deteriorates the squareness of I–V curve, consequently decreases the FF [25]. The increase in series resistance reflects poor charge collection efficiency, and reduction in shunt resistance indicates increase in charge transport hindrance due to increased recombination in the thick active layer OSC.

In order to understand the affect of active layer thickness on the photovoltaic performance, we further carried out the C–V characteristics of the OSCs. The measured capacitance for different active layer thickness as a function of applied forward voltage is shown in Fig. 4(b). Initially, the capacitance increases with the increase in the applied voltage up to the peak value, and then decreases instantly. The peak voltage (V_p) is related to the built-in voltage (V_{bi}) through the relation, $V_p \propto V_{bi} - k_B T/e$. Below built-in voltage, the diffusion of charge carriers accumulate space charge near the injecting electrode, which gives rise to the increase in capacitance [26]. Beyond built-in voltage, the accumulated space charge carriers drift under the influence of the applied electric field, and extracted through the device, as a consequence device capacitance reduces [27]. In addition to the extraction of charges, the decrease in capacitance can also be caused by the recombination of carriers inside the photoactive layer [28]. The peak voltage depends on the active layer thickness and show the same trend, as the open circuit voltage (Table 1). The more frequent charge recombination in the comparatively thick active layer (200 nm) causes reduction in the peak voltage, and hence results in the lowest V_{OC} .

Next, we analyze the dark J–V characteristics under the framework of Shockley model. The dark J–V characteristics reveal the role of ideality factor and reverse saturation current on the development of the photovoltaic parameters of OSCs. The reverse saturation current (I_0) can be determined from the extrapolating and finding the value of intercept on y axis in semi-logarithmic dark J–V characteristics shown in Fig. 4(a). Ideality factor (η) can be deduced from the slope of forward semi-logarithmic J–V curve as

$$\eta = \left(\frac{kT}{q} \frac{\partial \ln J}{\partial V} \right) \quad (2)$$

The estimated value of the ideality factor and reverse saturation are listed in Table 2.

It can be apparent that the η increases with enlarging the active layer thickness, while I_0 estimated to be minimum for active layer thickness of 150 nm and largest for 200 nm for active layer thickness of 150 nm.

The ideality factor describes recombination behavior of the devices. Therefore it provides information regarding the interface and trap density, and may characterize morphology of the active layer [29,30]. The ideality factor larger than 1 can be attributed to the trap assisted recombination in OSC. The increase in ideality factor with active layer thickness implies increase in the defect density, which in turn creates different recombination pathways for charge carriers. The comparatively larger ideality factor observed for the device with 200 nm active layer thickness indicates large density of defect states causing the trap assisted recombination process to dominate, which can be the main reason for sharp drop in the fill factor (Table 1).

On the other hand, parameter I_0 arises due to the thermal generation of charge carriers over the energetic barrier when an electron is transferred from the donor HOMO level to the charge transfer state in the acceptor at the heterojunction [31,32]. I_0 is governed by the diffusion and recombination of charge carrier. The existence of defects promotes recombination and hence increases I_0 . larger I_0

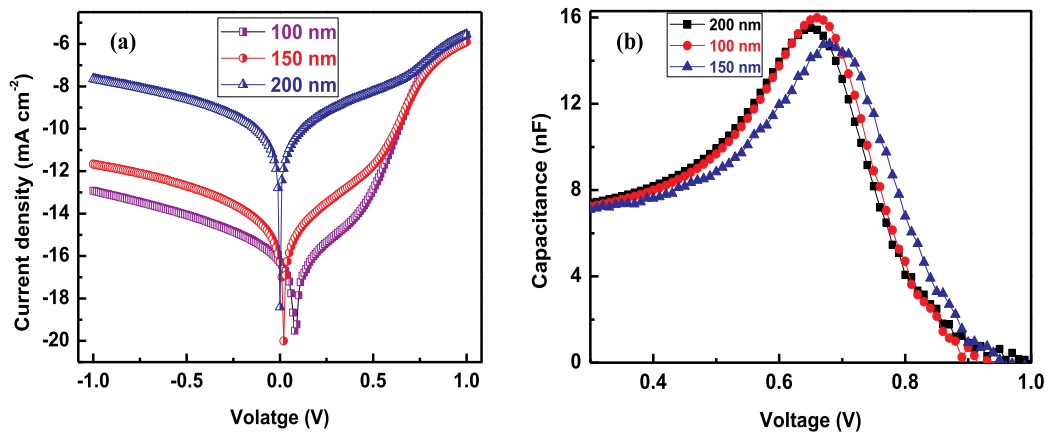


Fig. 4. (a) The semi-logarithmic J–V characteristics of PTB7:PC70BM BHJ OSCs for different active layer thickness measured under dark condition, (b) C–V characteristics of PTB7:PC70BM BHJ OSCs as a function of active layer thickness.

Table 2

Comparison of diode parameters of OSCs with different active layer thickness extracted from the I–V curves.

S. No.	Active layer thickness	I_0 (Amp.)	η
1.	100 nm	3.6×10^{-9}	1.59
2.	150 nm	1.94×10^{-9}	1.98
3.	200 nm	9.8×10^{-9}	4.96

observed in the device with 200 nm active layer thickness is due to the comparatively large defects in the active layer, causing dominance of bulk recombination over the other recombination processes [33]. The effect of I_0 is can be related to V_{oc} by Eq. (1), which clearly explains why V_{oc} dropped at $t = 200$ nm.

Further, leakage current density of the OSC continuously increases with increase in thickness of the active layer, as can be clearly seen in Fig. 4(a). The generation of leakage current can be attributed to the defects including pin holes and traps, which can act as the recombination centers and thus form path for the current leakage [34]. In BHJ blends, the charge traps and defects arises due to nano-scale morphology of isolated networks opposed to bicontinuous morphology [35–38]. The chances of more isolated phase separated domains is larger in thicker active layer device, which leads to increased charge trapping and hence greater chances of recombination. In thinner active layer device, the chances of such isolated phase separated domains is less, thus have low recombination losses. The leakage current reduces the current flowing through the load, as a consequence net photo current in the OSC decreases. The increase in recombination sites with the active layer thickness raises the leakage current, leading to reduction in the contact selectivity, consequently reduces R_{SH} (see Table 1), which in turn adversely affects the fill factor and PCE of OSCs [39].

To gain the deeper understanding on the active layer thickness dependence on the photovoltaic performance, impedance spectra (IS) of OSCs were acquired and results are presented in Fig. 5 (a) & (b) in terms of Nyquist plot, and in Fig. 5(c) in terms of Bode phase plot. The electrical equivalent circuit [Fig. 5(d) and (e)], which provide description about the charge transport and recombination processes occurring inside the device is employed to the fit the impedance results and to extract the relevant parameters. The extracted key impedance parameters are summarized in Table 3. Measured IS data of the device with $t = 100$ nm show good fit with the R-RC circuit. However, R-RC-RC circuit yield better fit for $t = 150$ nm and $t = 200$ nm. First parallel RC [Fig. 5 (d)] circuit reflects the feature of low frequency side in the Nyquist plot, corresponding to the charge recombination process taking place inside the device, whereas high frequency response of the OSCs is associated with charge transport processes and is modeled by the second parallel RC [Fig. 5 (e)]

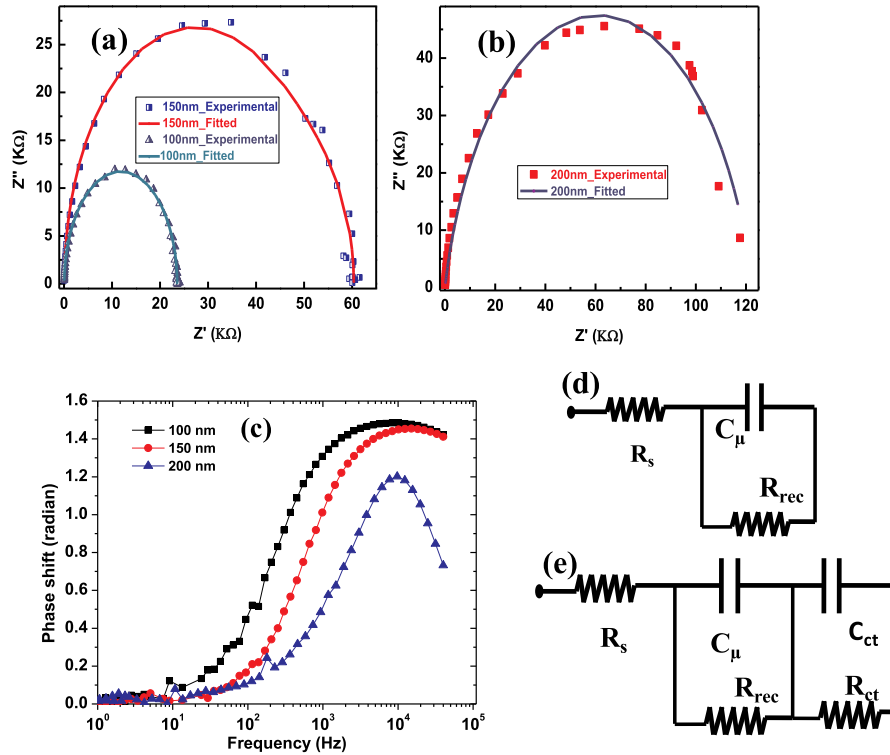


Fig. 5. Impedance spectra of the OSCs with corresponding fitted curves, Nyquist plots for (a) active layer thickness of 100 nm and 150 nm (b) active layer thickness of 200 nm, and (c) Bode phase plot. The electrical equivalent circuit utilized for fitting the experimental data for the devices of (d) 100 nm active layer thickness, and (e) active layer thickness of 150 nm and 200 nm.

Table 3

Extracted impedance parameters of OSCs with different active layer thickness.

S.No.	active layer thickness	$R_s(\Omega)$	$R_{rec}(k\Omega)$	$C_{\mu}(F)$	$R_{ct}(k\Omega)$	$C_{ct}(F)$	τ (s) ($R_{rec}(\Omega) \times C_{\mu}(F)$)	τ (s) (Bode phase plot)
1	100 nm	60.282	2.35	4.34×10^{-9}	–	–	1.02×10^{-4}	0.96×10^{-4}
2	150 nm	55.8	4.90	5.04×10^{-9}	1.13	1.06×10^{-7}	2.4×10^{-4}	2.04×10^{-4}
3	200 nm	108.05	3.35	4.23×10^{-9}	8.37	1.20×10^{-8}	1.76×10^{-4}	1.02×10^{-4}

network in electrical equivalent circuit [40].

The impedance parameters are explicitly labeled according to the respective processes, as depicted in Fig. 5(d) and (e). R_s represents series resistance, which include contribution from connector leads, and metal contacts. R_{ct} denotes charge transport resistance, that determines the effectiveness of charge transport through the device and depends on the carrier transport mechanisms such as diffusion and drift, and C_{ct} stand for the interfacial capacitance [41], R_{rec} is recombination resistance related to the recombination of charge carriers during transport and it is inversely proportional to the recombination rate [42], and C_{μ} being the chemical capacitance, which reveal how much effective the device is in releasing and accepting excess carriers upon change in the Fermi levels [38,43]. The carrier life time (τ) was estimated as, $\tau = R_{rec} \times C_{\mu}$. The carrier life time for different active layer thickness was also determined from the Bode phase plot shown in Fig. 5(c). The extracted impedance parameters are listed in Table 3.

The absence of second RC circuit in the electrical equivalent circuit of OSC with $t = 100$ points to an indication that the charge transport process is not the main performance limiting factor at less t . As can be seen in Table 3, OSC with $t = 150$ nm exhibits large recombination resistance compared to the OSC with $t = 100$ nm and $t = 200$ nm, indicating less charge recombination events, leading to the best value of J_{sc} , V_{OC} and PCE. However, electrical equivalent circuit of OSC with $t = 150$ nm shows charge transport resistance in addition to recombination resistance, suggesting charge transport hampering in the active layer, causing reduction in charge collection efficiency [39,44], which explains reduction in FF for OSC with $t = 150$ nm compared to OSC having $t = 100$ nm [45]. OSC having $t = 200$ nm exhibits less recombination resistance than OSC with $t = 150$ nm, implying increase in the recombination sites for the OSC with $t = 200$ nm. This is in consistent with the increase in the defect density with increase in the active layer thickness, as observed in the dark current analysis. Additionally, large difference in transport resistance shown by device OSC $t = 200$ nm and $t = 150$ nm may be ascribed mainly to the dissimilarity in the dominant transport mechanism. In the OSC with $t = 200$ nm, thick active layer weakens the electric field and increase electric field free zone, causing diffusive transport to dominant, while in OSC with $t = 150$ nm both diffusive and drift play important role in the transport of photo generated carriers. Comparatively slow diffusive transport therefore causes higher charge transport resistance in OSC with $t = 200$ nm [46]. Larger charge transport resistance and smaller recombination resistance may explain why the OSC with $t = 200$ nm shows poor photovoltaic performance compared than OSC with $t = 100$ nm and $t = 150$ nm, that can be clearly seen in Table 1 and Fig. 3.

4. Conclusions

In conclusion, the inverted BHJ organic solar cells of the different active layer thickness were fabricated to understand the thickness dependence of photovoltaic parameters, including J_{sc} , V_{OC} , FF, and PCE. Capacitance-voltage (C–V), dark current-voltage (I–V) and impedance spectroscopy (IS) analysis were carried out to explain the observed thickness dependence of photovoltaic performance. The short circuit photocurrent density (J_{sc}) first increases by the change in the active layer thickness from 100 to 150 nm and then found to decrease when thickness changed to 200 nm. An initial rise in J_{sc} was mainly related to enhancement in the absorption upon increase in the active layer thickness. However, despite the better absorption at 200 nm thick layer, increased charge recombination and poor interface quality hampered the charge transport and charge transfer, which in turn diminished the J_{sc} . The dark I–V analysis revealed that charge recombination and the leakage current was significantly enhanced due to the higher defect density for the device having active layer thickness of 200 nm. The increased recombination and larger leakage current at 200 nm drastically reduce FF, which lead to the significant decline in the photovoltaic performance. From IS analysis, It was observed that the increase in transport resistance due to the diffusing character of transport, and lesser charge recombination resistance limits the OSC efficiency at large active layer thickness.

Acknowledgment

The authors gratefully acknowledge financial support from DST, India under CURIE program (grant No. SR/CURIE- Phase-III/01/2015(G)) and MHRD FAST Programme (grant No.5-5/2014-TS.VII), Govt. of India.

Appendix A. Supplementary data

Supplementary data to this article can be found online at <https://doi.org/10.1016/j.spmi.2019.106278>.

References

- [1] K. Masuko, M. Shigematsu, T. Hashiguchi, D. Fujishima, M. Kai, N. Yoshimura, T. Yamaguchi, Y. Ichihashi, T. Mishima, N. Matsubara, T. Yamanishi, T. Takahama, M. Taguchi, E. Maruyama, S. Okamoto, Achievement of more than 25% conversion efficiency with crystalline silicon heterojunction solar cell, *IEEE J Photovoltaics* 4 (2014) 1433–1435, <https://doi.org/10.1109/JPHOTOV.2014.2352151>.
- [2] M. Sharma, P.R. Pudasaini, F. Ruiz-Zepeda, D. Elam, A.A. Ayon, Ultrathin, flexible organic-inorganic hybrid solar cells based on silicon nanowires and PEDOT: PSS, *ACS Appl. Mater. Interfaces* 6 (2014) 4356–4363, <https://doi.org/10.1021/am500063w>.
- [3] G. Keru, P.G. Ndungu, V.O. Nyamori, A review on carbon nanotube/polymer composites for organic solar cells, *Int. J. Energy Res.* 38 (2014) 1635–1653, <https://doi.org/10.1002/er.3194>.
- [4] M. Pagliaro, R. Criminna, G. Palmisano, Flexible solar cells, *ChemSusChem* 11 (2008) 880–891, <https://doi.org/10.1002/cssc.200800127>.
- [5] E. Kabir, P. Kumar, S. Kumar, A.A. Adelodun, K.H. Kim, Solar energy: potential and future prospects, *Renew. Sustain. Energy Rev.* 82 (2018) 894–900, <https://doi.org/10.1016/j.rser.2017.09.094>.
- [6] N. Sharma, C. Mohan, S. Negi, A.S. Verma, S.K. Gupta, C60 concentration influence on MEH-PPV:C60 bulk heterojunction-based Schottky, *Devices* 47 (2018) 7023–7033, <https://doi.org/10.1007/s11664-018-6629-3>.
- [7] M. Ramirez-Como, V.S. Balderrama, A. Sacramento, L.F. Marsal, G. Lastra, M. Estrada, Fabrication and characterization of inverted organic PTB7:PC 70 BM solar cells using HF-In-ZnO as electron transport layer, *Sol. Energy* 181 (2019) 386–395, <https://doi.org/10.1016/j.solener.2019.02.015>.
- [8] J. Kniepert, I. Lange, J. Heidbrink, J. Kurpiers, T.J.K. Brenner, L.J.A. Koster, D. Neher, Effect of solvent additive on generation, recombination, and extraction in PTB7:PCBM solar cells: A conclusive experimental and numerical simulation study, *J. Phys. Chem. C* 119 (2015) 8310–8320, <https://doi.org/10.1021/jp512721e>.
- [9] P. Rathore, C.M.S. Negi, A.S. Verma, A. Singh, G. Chauhan, A.R. Inigo, S.K. Gupta, Investigation of the optical and electrical characteristics of solution-processed poly (3 hexylthiophene) (P3HT):multiwall carbon nanotube (MWCNT) composite-based devices, *Mater. Res. Express* 4 (2017), 085905, <https://doi.org/10.1088/2053-1591/aa7dac>.
- [10] L. Lu, T. Xu, W. Chen, J.M. Lee, Z. Luo, I.H. Jung, H. Il Park, S.O. Kim, L. Yu, The role of N-doped multiwall carbon nanotubes in achieving highly efficient polymer bulk heterojunction solar cells, *Nano Lett.* 13 (2013) 2365–2369, <https://doi.org/10.1021/nl304533j>.
- [11] B. Liu, X. Chen, Y. Zou, Y. He, L. Xiao, X. Xu, L. Li, Y. Li, A benzo[1,2-b:4,5-b']difuran- and thieno-[3,4-b]thiophene-based low bandgap copolymer for photovoltaic applications, *Polym. Chem.* 4 (2013) 470–476, <https://doi.org/10.1039/c2py20580g>.
- [12] Y.J. Hsieh, Y.C. Huang, W.S. Liu, Y.A. Su, C.S. Tsao, S.P. Rwei, L. Wang, Insights into the morphological instability of bulk heterojunction PTB7-Th/PCBM solar cells upon high-temperature aging, *ACS Appl. Mater. Interfaces* 9 (2017) 14808–14816, <https://doi.org/10.1021/acsami.7b01296>.
- [13] M. Gerhard, A.P. Arndt, M. Bilal, U. Lemmer, M. Koch, I.A. Howard, Field-induced exciton dissociation in PTB7-based organic solar cells, *Phys. Rev. B* 95 (2017) 1–12, <https://doi.org/10.1103/PhysRevB.95.195301>.
- [14] Y. Li, Y. Liu, Z. Liu, X. Xie, E.C. Lee, Improvement of inverted organic solar cells using acetic acid as an additive for ZnO layer processing, *AIP Adv.* 8 (2018), <https://doi.org/10.1063/1.5018382>.
- [15] S.H. Liao, H.J. Jhuo, Y.S. Cheng, V. Gupta, S.A. Chen, A high performance inverted organic solar cell with a low band gap small molecule (p-DTS(FBTTh₂))₂ using a fullerene derivative-doped zinc oxide nano-film modified with a fullerene-based self-assembled monolayer as the cathode, *J. Mater. Chem.* 3 (2015) 22599–22604, <https://doi.org/10.1039/c5ta05216e>.
- [16] J. Khanam, S. Foo, Modeling of high-efficiency multi-junction polymer and hybrid solar cells to absorb infrared light, *Polymers* 11 (2019) 383, <https://doi.org/10.3390/polym11020383>.
- [17] B. Ray, A.G. Baradwaj, M.R. Khan, B.W. Boudouris, M.A. Alam, Collection-limited theory interprets the extraordinary response of single semiconductor organic solar cells, *Proc. Natl. Acad. Sci.* 112 (2015) 11193–11198, <https://doi.org/10.1073/pnas.1506699112>.
- [18] Y. Zheng, G. Wang, D. Huang, J. Kong, T. Goh, W. Huang, J. Yu, A.D. Taylor, Binary solvent additives treatment boosts the efficiency of PTB7:PCBM polymer solar cells to over 9.5%, *Sol RRL* 2 (2018) 1870161, <https://doi.org/10.1002/solr.201870161>.
- [19] T. Kirchartz, T. Agostinelli, M. Campoy-Quiles, W. Gong, J. Nelson, Understanding the thickness-dependent performance of organic bulk heterojunction solar cells: the influence of mobility, lifetime, and space charge, *J. Phys. Chem. Lett.* 3 (2012) 3470–3475, <https://doi.org/10.1021/jz301639y>.
- [20] Y. Min Nam, J. Huh, W. Ho Jo, Optimization of thickness and morphology of active layer for high performance of bulk-heterojunction organic solar cells, *Sol. Energy Mater. Sol. Cells* 94 (2010) 1118–1124, <https://doi.org/10.1016/j.solmat.2010.02.041>.
- [21] Y. Liang, Z. Xu, J. Xia, S.T. Tsai, Y. Wu, G. Li, C. Ray, L. Yu, For the bright future-bulk heterojunction polymer solar cells with power conversion efficiency of 7.4%, *Adv. Mater.* 22 (2010) 135–138, <https://doi.org/10.1002/adma.200903528>.
- [22] D. Huang, Y. Li, Z. Xu, S. Zhao, L. Zhao, J. Zhao, Enhanced performance and morphological evolution of PTB7:PC71BM polymer solar cells by using solvent mixtures with different additives, *Phys. Chem. Phys.* 17 (2015) 8053–8060, <https://doi.org/10.1039/c4cp05826g>.
- [23] M. Mohan, V. Nandal, S. Paramadam, K.P. Reddy, S. Ramkumar, S. Agarwal, C.S. Gopinath, P.R. Nair, M.A.G. Nambhoorthy, Efficient organic photovoltaics with improved charge extraction and high short-circuit current, *J. Phys. Chem. C* 121 (2017) 5523–5530, <https://doi.org/10.1021/acs.jpcc.7b01314>.
- [24] A. Mauroan, R. Hamilton, C.G. Shuttle, A.M. Ballantyne, J. Nelson, B. O'Regan, W. Zhang, I. McCulloch, H. Azimi, M. Morana, C.J. Brabec, J.R. Durrant, Recombination dynamics as a key determinant of open circuit voltage in organic bulk heterojunction solar cells: a comparison of four different donor polymers, *Adv. Mater.* 22 (2010) 4987–4992, <https://doi.org/10.1002/adma.201002360>.
- [25] B. Qi, J. Wang, Fill factor in organic solar cells, *Phys. Chem. Phys.* 15 (2013) 8972–8982, <https://doi.org/10.1039/c3cp51383a>.
- [26] K.G. Lim, H.B. Kim, J. Jeong, H. Kim, J.Y. Kim, T.W. Lee, Boosting the power conversion efficiency of perovskite solar cells using self-organized polymeric hole extraction layers with high work function, *Adv. Mater.* 26 (2014) 6461–6466, <https://doi.org/10.1002/adma.201401775>.
- [27] D.C. Tripathi, Y.N. Mohapatra, Diffusive capacitance in space charge limited organic diodes: Analysis of peak in capacitance-voltage characteristics, *Appl. Phys. Lett.* 102 (2013), <https://doi.org/10.1063/1.4812487>.
- [28] K.G. Lim, M.R. Choi, J.H. Kim, D.H. Kim, G.H. Jung, Y. Park, J.L. Lee, T.W. Lee, Role of ultrathin metal fluoride layer in organic photovoltaic cells: Mechanism of efficiency and lifetime enhancement, *ChemSusChem* 7 (2014) 1125–1132, <https://doi.org/10.1002/cssc.201301152>.
- [29] M.A. Kroon, R.A.C.M.M. Van Swaaij, Spatial effects on ideality factor of amorphous silicon pin diodes, *J. Appl. Phys.* 90 (2001) 994–1000, <https://doi.org/10.1063/1.1379560>.
- [30] A. Upadhyaya, C.M.S. Negi, A. Yadav, S.K. Gupta, A.S. Verma, Synthesis and characterization of methylammonium lead iodide perovskite and its application in planar hetero-junction devices, *Semicond. Sci. Technol.* 33 (2018) 65012, <https://doi.org/10.1088/1361-6641/aac066>.
- [31] W.J. Potscavage, S. Yoo, B. Kippelen, Origin of the open-circuit voltage in multilayer heterojunction organic solar cells, *Appl. Phys. Lett.* 93 (2008) 2008–2010, <https://doi.org/10.1063/1.3027061>.
- [32] B. Kitchen, O. Awartani, R.J. Kline, T. McAfee, H. Ade, B.T. O'Connor, Tuning open-circuit voltage in organic solar cells with molecular orientation, *ACS Appl. Mater. Interfaces* 7 (2015) 13208–13216, <https://doi.org/10.1021/am508855s>.
- [33] Y. Zang, Q. Xin, J. Zhao, J. Lin, Effect of active layer thickness on the performance of polymer solar cells based on a highly efficient donor material of PTB7-Th, *J. Phys. Chem. C* 122 (2018) 16532–16539, <https://doi.org/10.1021/acs.jpcc.8b03132>.
- [34] M.H. Jao, H.C. Liao, W.F. Su, Achieving a high fill factor for organic solar cells, *J. Mater. Chem.* 4 (2016) 5784–5801, <https://doi.org/10.1039/c6ta00126b>.
- [35] S. Rath, G. Chauhan, S.K. Gupta, R. Srivastava, A. Singh, Analysis of blockade in charge transport across polymeric heterojunctions as a function of thermal annealing: a different perspective, *J. Electron. Mater.* 46 (2017) 1235–1247, <https://doi.org/10.1007/s11664-016-5097-x>.
- [36] W. Yin, M. Dadmun, A new model for the morphology of P3HT/PCBM organic photovoltaics from small-angle neutron scattering: rivers and streams, *ACS Nano* 5 (2011) 4756–4768, <https://doi.org/10.1021/nn200744q>.
- [37] B.A. Collins, J.R. Tumbleston, H. Ade, Miscibility, crystallinity, and phase development in P3HT/PCBM solar cells: toward an enlightened understanding of device morphology and stability, *J. Phys. Chem. Lett.* 2 (2011) 3135–3145, <https://doi.org/10.1021/jz2014902>.

- [38] S. Rathi, S.K. Gupta, C.M.S. Negi, A. Singh, Negative differential resistance in heterojunction polymeric films, *Superlattice Microstruct.* 114 (2018), <https://doi.org/10.1016/j.spmi.2017.10.010>.
- [39] C.M. Proctor, T.Q. Nguyen, Effect of leakage current and shunt resistance on the light intensity dependence of organic solar cells, *Appl. Phys. Lett.* 106 (2015), <https://doi.org/10.1063/1.4913589>.
- [40] A. Guerrero, N.F. Montcada, J. Ajuria, I. Etxebarria, R. Pacios, G. Garcia-Belmonte, E. Palomares, Charge carrier transport and contact selectivity limit the operation of PTB7-based organic solar cells of varying active layer thickness, *J. Mater. Chem.* 1 (2013) 12345–12354, <https://doi.org/10.1039/c3ta12358h>.
- [41] K. Park, Q. Zhang, D. Myers, G. Cao, Charge transport properties in TiO₂ network with different particle sizes for dye sensitized solar cells, *ACS Appl. Mater. Interfaces* 5 (2013) 1044–1052, <https://doi.org/10.1021/am302781b>.
- [42] H. Wang, Y. Wang, B. He, W. Li, M. Sulaman, J. Xu, S. Yang, Y. Tang, B. Zou, Charge carrier conduction mechanism in PbS quantum dot solar cells: electrochemical impedance spectroscopy study, *ACS Appl. Mater. Interfaces* 8 (2016) 18526–18533, <https://doi.org/10.1021/acsami.6b03198>.
- [43] J. Bisquert, Chemical capacitance of nanostructured semiconductors: its origin and significance for nanocomposite solar cells, *Phys. Chem. Chem. Phys.* 5 (2003) 5360–5364, <https://doi.org/10.1039/b310907k>.
- [44] L. Bertoluzzi, S. Ma, On the methods of calculation of the charge collection efficiency of dye sensitized solar cells, *Phys. Chem. Chem. Phys.* 15 (2013) 4283–4285, <https://doi.org/10.1039/c3cp44248a>.
- [45] P. Kaienburg, U. Rau, T. Kirchartz, Extracting information about the electronic quality of organic solar-cell absorbers from fill factor and thickness, *Phys Rev Appl* 6 (2016) 1–15, <https://doi.org/10.1103/PhysRevApplied.6.024001>.
- [46] L. Xu, Y.-J. Lee, J.W.P. Hsu, Charge collection in bulk heterojunction organic photovoltaic devices: An impedance spectroscopy study, *Appl. Phys. Lett.* 105 (2014) 123904, <https://doi.org/10.1063/1.4896633>.